

Entangled-to-Packed Crossover in Nonlinear Extensional Rheology of Entangled Polymers

Yin Wang[†], Lin-Feng Wu[†], Yi-Bo Shao, and Zhe Wang^{*}

Department of Engineering Physics and Key Laboratory of Particle and Radiation Imaging (Tsinghua University) of Ministry of Education, Tsinghua University, Beijing 100084, China

(Dated: December 1, 2025)

Significant challenges exist in the nonlinear extensional rheology of entangled polymers. With simulations, we show that the key to understanding this problem is to recognize the existence and importance of a strain-induced crossover from the entangled state to a packed state. This crossover, following the saturation of primitive chain stretch, takes place with massive release of entanglements via convective flow and progressive chain alignment. After the crossover, the disentangled, fully-aligned chain segments pack similarly to the random packing of rods. Meanwhile, the system enters the steady state. In this state, the tube model—built on the concept of entanglement—fails, while the stress can be quantitatively calculated by combining the intra-chain conformational contribution and a frictional contribution from the inter-chain separation along flow.

Entanglements profoundly influence the rheology of polymers [1–3]. By conceptualizing discrete entanglements as a continuous “tube”, the tube model significantly simplifies the many-body interaction among chains [1, 4]. With refinements such as constraint release [5, 6], and primitive length fluctuation [7, 8], the tube model successfully describes the linear rheology of polymers, enabling a universal description of rheological behaviors across diverse systems [9–12]. However, for the nonlinear extensional rheology, the validity of the tube model has been widely questioned in the past two decades [13–17]. For example, the aforesaid universality is found to be invalid in nonlinear extensional flows, as suggested by the observation that solutions and melts with the same number of entanglements per chain Z exhibit opposite trends in the steady-state extensional viscosity as a function of strain rate [16–22]. To meet this crisis, several mechanisms have been proposed, such as inter-chain pressure [23–25], nematic interaction [26–28], and friction reduction [29–34]. Even with these effects, tube model’s predictions still non-negligibly deviate from experimental and simulation results at large strains, especially in the steady state [35, 36]. These results call for a critical revision of the current theoretical picture for the nonlinear extensional flow of entangled polymers.

To tackle this problem, we examine the behaviors of entanglements during extension. Previous studies show that in nonlinear flows, Z may dramatically decrease with increasing strain [37–40]. Although this mechanism has been incorporated into tube models [40, 41], entanglements’ microscopic dynamics remain poorly understood, thereby impeding understanding the elusive phenomena observed in nonlinear extensional flows. With molecular dynamics (MD) simulations [42], we address the evolution of entanglements during the extensional flow, and its relation to the chain conformation, the inter-chain configuration, and most importantly, the rheology. We reveal

an entangled-to-packed crossover in inter-chain configuration and interaction as the strain surpasses a critical value, corresponding to a fundamental change in system’s rheological response: At small strains, the system is well entangled, and its response can be quantified by the tube model. During the crossover, chains massively disentangle by convection, accompanied by pronounced chain alignment. After the crossover, the disentangled, aligned chain segments pack similarly to the random packing of rods. Meanwhile, the system is in the steady state. In this state, the tube model fails due to the radical disentanglement, while the rheological response can be described by combining the effects of the intra-chain conformation and the inter-chain friction.

We simulate a series of entangled melts composed of N_c bead-spring chains with length N using LAMMPS [43]. All beads interact via the repulsive Lennard-Jones potential, and bonded beads are connected by the finite extensible nonlinear elastic (FENE) potential [44, 45]. Reduced units are adopted with energy ϵ , length σ , and time $\tau = \sigma(m/\epsilon)^{1/2}$, where m is the bead mass. The simulation is performed at temperature $T = 1$ and density $\rho = 0.85$. Extension along the z axis is applied under constant Hencky strain rate $\dot{\epsilon}_H$ [46–48]. To vary the equilibrium entanglement length N_e , we modulate the chain stiffness by adjusting the bending coefficient k_{bc} [49, 50]. Additional details are provided in the End Matter (EM). Z1+ algorithm [51] is used to identify primitive paths (PP) of chains and entanglements. Strain rate is represented by Rouse Weissenberg number $Wi_R = \dot{\epsilon}_H \tau_R$, where τ_R is the chain Rouse time. Wi_R is kept at $Wi_R \gg 1$ to ensure strong nonlinear response.

Figure 1(a) shows the evolutions of Z during extension with a fixed N_e and various Wi_R and N . In all cases, Z exhibits an initial plateau, and starts to disentangle as the Hencky strain ϵ_H surpasses a critical value ϵ_{H1} . Seen from Fig. 1(a), ϵ_{H1} is independent on N and Wi_R . Figure 1(b) examines the evolutions of Z with different N_e , revealing a strong increase of ϵ_{H1} on N_e . To clarify this origin of the disentanglement, we check the mean PP length \bar{L}_{pp} as a function of the stretch ratio $\lambda = e^{\epsilon_H}$,

* [†] These authors contributed equally to this work; * Corresponding author; zwang2017@mail.tsinghua.edu.cn

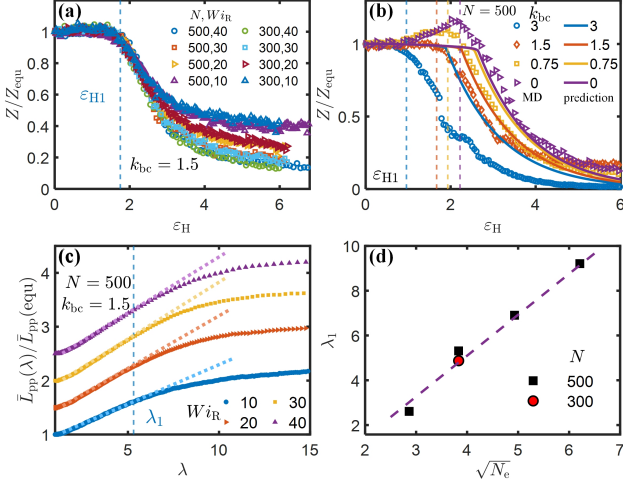


FIG. 1. $Z(\varepsilon_H)$, normalized by equilibrium value Z_{equ} , for the conditions of (a) $k_{bc} = 1.5$, $N = 300$ and 500 , $W_{iR} = 10 - 40$, and (b) $N = 500$, $W_{iR} = 40$, $k_{bc} = 0 - 3$. Symbols: MD results; lines: model [40] predictions (with CCR parameter $\beta = 0.8$). (c) PP length growth $\bar{L}_{pp}(\lambda)$ normalized by equilibrium value $\bar{L}_{pp}(\text{equ})$ for the sample of $N = 500$ and $k_{bc} = 1.5$ at $W_{iR} = 10 - 40$. Data are vertically shifted for clarity. In (a) – (c), the positions of ε_{H1} or λ_1 are denoted by vertical dashed lines. (d) The critical stretch ratio λ_1 versus $\sqrt{N_e}$.

and show the results of a sample in Fig. 1(c). At small strains, \bar{L}_{pp} linearly grows with λ , indicating an affine deformation. As λ surpasses $\lambda_1 = e^{\varepsilon_{H1}}$, the extension of \bar{L}_{pp} deviates from linearity and starts to saturate. The saturation of \bar{L}_{pp} signifies the breakdown of affine deformation, suggesting that the further extension involves significant sliding between chains, which leads to the release of entanglements. The sliding between chains has been attributed to the imbalance between inter-chain grip force and retraction force [52–54]. Considering that the maximum stretch ratio of PP is proportional to $N_e^{1/2}$ [55], we expect a relation of $\lambda_1 \sim N_e^{1/2}$. This relation is confirmed in Fig. 1(d) with different samples. By employing the concept of convective constraint release (CCR) [56–58], the loss of entanglement is modeled [40], and the modeling results are also plotted in Fig. 1(b). It is seen that the CCR model qualitatively captures the features of the decay of Z observed in our MD simulation. The importance of convection in entanglement loss will be further clarified in following parts.

To further investigate the stretch-induced disentanglement, we focus on local structure and motion of entanglements during extension. It should be noted that not all entanglements found by PP identification methods, such as the Z1+ algorithm, effectively contribute to the stress in deformed polymers [59–62]. To account for this effect, we propose the concept of effective entanglement (EE) recently [59]. For a stretched chain, whether the l th entanglement is an EE depends on the configuration

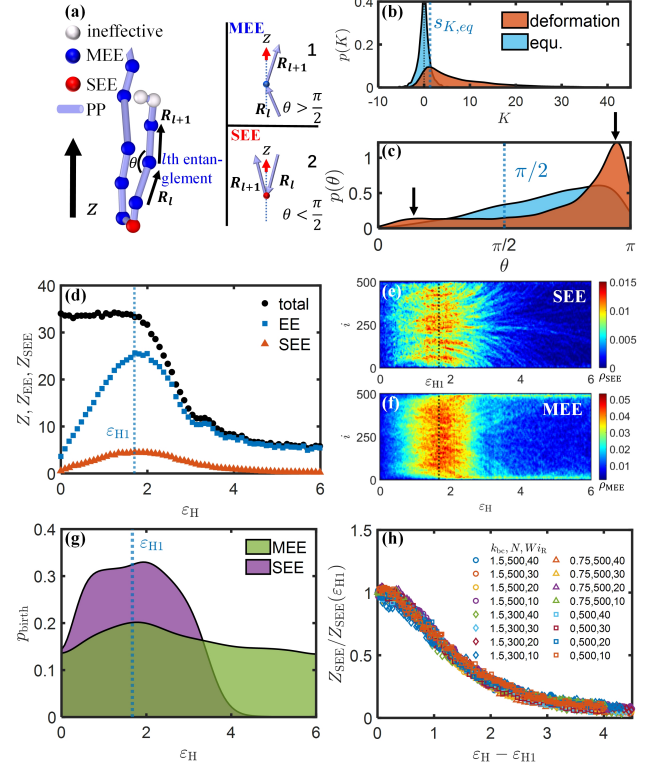


FIG. 2. Properties of EE. (a) Illustration of SEE, MEE and ineffective entanglement in a segment of PP stretched to ε_{H1} . (b) and (c) respectively give the distributions of K and θ at equilibrium and at ε_{H1} . (d) Evolutions of total number of entanglements (Z), EE (Z_{EE}), and SEE (Z_{SEE}) per chain during extension. (e) and (f) respectively give the density of entanglements $\rho(i, \varepsilon_H)$ along chain's monomer coordinate i as a function of ε_H for SEE and MEE. (g) Comparison between the distributions of birth time of SEE and MEE during extension. Data in (a) – (g) are measured with the sample of $N = 500$ and $k_{bc} = 1.5$ at $W_{iR} = 40$. (h) Decay of SEE at $\varepsilon_H \geq \varepsilon_{H1}$ as a function of strain under various conditions.

of its two associated strands, reflected by a parameter K :

$$K(l) = \frac{R_{l,z}^2 - R_{l,x}^2}{N_{s,l}} + \frac{R_{l+1,z}^2 - R_{l+1,x}^2}{N_{s,l+1}}, \quad (1)$$

where $R_{l,x/z}$ is the x/z component of the end-to-end vector \mathbf{R}_l of the l th strand in a chain, and $N_{s,l}$ is the number of monomers in the l th strand, as illustrated in Fig. 2(a). Seen from Fig. 2(b), as stretch is applied, the distribution of K deviates from the equilibrium form and shifts to larger values. An entanglement is identified as an EE if its K is larger than the standard deviation $s_{K,\text{eq}}$ of the equilibrium K distribution [59], which suggests that the conformation of its two strands effectively align with the flow direction and contribute to the conformational tensile stress $\sigma_t \sim \sum_l (R_{l,z}^2 - R_{l,x}^2)/N_{s,l}$.

Entanglements with sharp angles have been discussed in literature, with observations highlighting their roles in the mechanical response of stretched polymers [61–65].

For an EE, its angle θ is given by $\cos \theta = -\hat{\mathbf{R}}_l \cdot \hat{\mathbf{R}}_{l+1}$. According to θ , we classify all EEs into two types: sharp EE (SEE) with $\theta \leq \pi/2$, and mild EE (MEE) with $\theta > \pi/2$. In Fig. 2(a), we mark SEEs and MEEs in a PP of a stretched sample. The distributions of θ ($p(\theta)$) before and after a stretch to ε_{H1} are shown in Fig. 2(c). The stretch causes $p(\theta)$ to change from a unimodal form to a bimodal form, whose two peaks respectively correspond to SEE and MEE. Figure 2(d) shows the evolutions of total entanglements (Z), EEs (Z_{EE}), and SEEs (Z_{SEE}) per chain of a stretched sample. Both Z_{EE} and Z_{SEE} increase with ε_H in the beginning of extension due to chain orientation and stretching, and start to decrease at ε_{H1} . At $\varepsilon_H > \varepsilon_{H1}$, most entanglements become effective due to the strong alignment of chains. To examine the emergence and motion of EE, we calculate the local density of EE $\rho(i, \varepsilon_H)$ along the chain monomer coordinate i (i represents the i th monomer of a chain) as a function of ε_H . Figure 2(e) and (f) show the results of $\rho(i, \varepsilon_H)$ for SEE and MEE, respectively. Using the local maxima of $\rho(i, \varepsilon_H)$ to pinpoint the birth events of EEs, we obtain the distribution of birth event as a function of ε_H for SEE and MEE, and show the results in Fig. 2(g). At $\varepsilon_H > \varepsilon_{H1}$, the birth of SEE becomes rarer and rarer as ε_H increases. Due to the acute feature, an SEE typically appears at the corner of a Z-fold PP, as illustrated in Fig. 2(a). Thus, the creation of an SEE requires a coiled conformation of the fragment of PP, which is increasingly suppressed as the chain alignment enhances. For an MEE, in contrast, the end-to-end vectors of its two associated strands are oriented to similar directions that are nearly parallel to the flow, as illustrated in Fig. 2(a). Consequently, MEEs can be generated even when chains are highly aligned. As seen in Fig. 2(g), MEE maintains stable formation rate at $\varepsilon_H > \varepsilon_{H1}$. Additionally, at $\varepsilon_H > \varepsilon_{H1}$, most MEEs frequently appear and release at chain ends due to fluctuations, as shown in Fig. 2(f). Therefore, MEEs form a “dynamic background” contribution to the total number of entanglements at large strains. On the other hand, as shown in Fig. 2(e), SEEs show clear outward-sliding trajectories along the PP as strain proceeds, revealing the convective origin of their release.

As discussed above, beyond ε_{H1} , SEEs are of significant geometrical importance and are rare to be regenerated, thus serving as an indicator for probing the disentangling process. In Fig. 2(h), we plot the decay of $Z_{SEE}(\varepsilon_H)$ at $\varepsilon_H > \varepsilon_{H1}$, normalized at $\varepsilon_H = \varepsilon_{H1}$, for different samples and flow rates. It is seen that all data collapse onto a master curve, suggesting that the disentangling process takes place through the convection of flow. A model for the convective decay of $Z_{SEE}(\varepsilon_H)$ is provided in the EM.

With progressive stretching, the population of SEEs diminishes to nearly zero, meanwhile the chain conformation gradually achieves full-chain alignment. To examine the influence of these phenomena on the inter-chain configuration, we calculate the 2-dimensional (2D) pair distribution function $g_{2D}(r)$ of chains. To be spe-

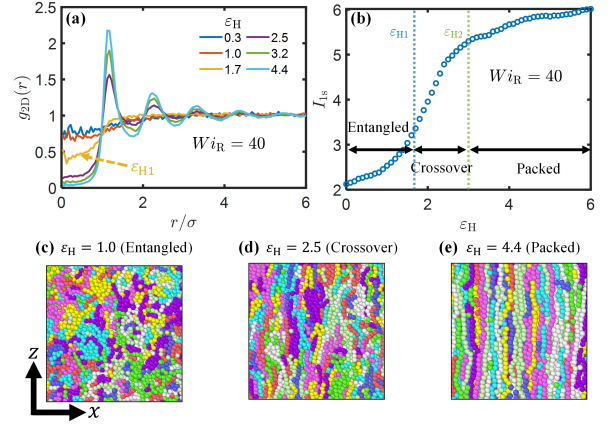


FIG. 3. Structural evolution of the sample of $N = 500$ and $k_{bc} = 1.5$ at $Wi_R = 40$. (a) Evolution of $g_{2D}(r)$ during extension. (b) I_{1s} as a function of ε_H . Two critical strains, ε_{H1} and ε_{H2} , are denoted by vertical dashed lines. (c) – (e) respectively show the snapshots of chains at $\varepsilon_H = 1.0$, 2.5 , and 4.4 .

cific, we first partition the system into slices along flow direction with certain thickness. Then, for each slice, we project the centers of mass of chain segments within this slice onto the $x - y$ plane. With these projected points, $g_{2D}(r)$ can be calculated (see EM). Figure 3(a) shows the evolution of $g_{2D}(r)$ of a sample as ε_H increases with $Wi_R = 40$. At $\varepsilon_H > \varepsilon_{H1}$, $g_{2D}(r)$ gradually develops a pronounced peak, corresponding to a well-defined first coordination shell. With $g_{2D}(r)$, we calculate the average chain number in the first shell I_{1s} . As shown in Fig. 3(b), I_{1s} rapidly grows with ε_H when $\varepsilon_H > \varepsilon_{H1}$, and starts to saturate to a plateau value close to 6 when ε_H exceeds another critical value ε_{H2} . The behavior of $g_{2D}(r)$ at $\varepsilon_H > \varepsilon_{H2}$ exhibits typical features of 2D random packing [66]. Figure 3(c)-(e) respectively display the chains of a sample stretched to $\varepsilon_H = 1$ ($< \varepsilon_{H1}$), 2.5 ($\varepsilon_{H1} < \varepsilon_H < \varepsilon_{H2}$) and 4.4 ($> \varepsilon_{H2}$) with $Wi_R = 40$, whose difference visualizes the entangled-to-packed crossover in the inter-chain configuration, as suggested by the behaviors of $g_{2D}(r)$. Seen from Fig. 2, a few MEEs still exist at $\varepsilon_H > \varepsilon_{H2}$, while they are rapidly fluctuating and well aligned with the flow, thereby hardly affecting the packed structure. Note that, some studies have implied the emergence of the packed state at large strains but lack systematic demonstration and analysis [32, 55, 67, 68]. Our work clearly shows the existence of such state, and how it is induced by the strong extensional flow.

In the packed state, concepts built on entanglements, such as N_e and the reptation time τ_d , lose their structural basis. This explains why the tube model cannot give a satisfactory description on the nonlinear extensional rheology. Figure 4(a) shows the stress-strain data of a sample at different Wi_R . The total tensile stress σ_{tot} , calculated by the Virial expression [44, 50], enters

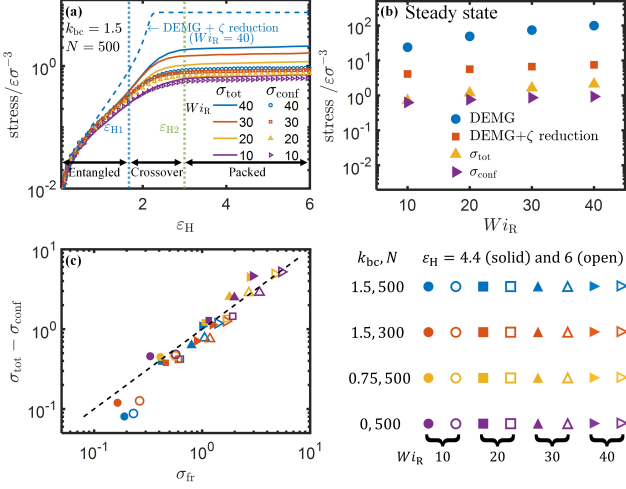


FIG. 4. Tensile stress. (a) Total stress σ_{tot} and conformational stress σ_{conf} as a function of $\dot{\epsilon}_H$ for the sample of $N = 500$ and $k_{bc} = 1.5$ at $Wi_R = 10 - 40$. DEMG prediction with friction reduction is also given (dashed line). (b) σ_{tot} , σ_{conf} , and DEMG predictions (with and without friction reduction) at steady states as a function of Wi_R for the sample of $N = 500$ and $k_{bc} = 1.5$. (c) Scatter plot between $\Delta\sigma = \sigma_{\text{tot}} - \sigma_{\text{conf}}$ and frictional stress σ_{fr} (eq. 3) for various steady-state conditions denoted in the right side of panel. The dashed line denotes $\Delta\sigma = \sigma_{fr}$.

the steady state at $\dot{\epsilon}_H > \dot{\epsilon}_{H2}$ where both the chain conformation and inter-chain configuration become steady. The result at $Wi_R = 40$ predicted by the DEMG model supplemented by FENE and friction reduction (see EM) [69, 70] is also shown in Fig. 4(a). The theoretical result remarkably deviates from the MD result at $\dot{\epsilon}_H > \dot{\epsilon}_{H1}$, suggesting the failure of the tube model. An alternative picture is, thus, in need. To seek this picture, we first calculate the conformational stress via the stress-optical rule (SOR) by [71–74]:

$$\sigma_{\text{conf}} = \frac{\sum_{i=1}^{N_c} \sum_{j=1}^{N-1} [u_{ij}^z u_{ij}^z - \frac{1}{2} (u_{ij}^x u_{ij}^x + u_{ij}^y u_{ij}^y)]}{\alpha V}, \quad (2)$$

where u_{ij}^β is the β component of the j th bond vector in the i th chain. The parameter α is determined by equating σ_{conf} to the Virial result σ_{tot} in the low-strain regime where the SOR holds [74, 75]. The results of σ_{conf} are also given in Fig. 4(a). σ_{conf} and σ_{tot} exhibit nonnegligible difference at $\dot{\epsilon}_H > \dot{\epsilon}_{H1}$, which is enhanced as Wi_R increases. The systematic difference between σ_{conf} and σ_{tot} in the steady state, and that between MD results and DEMG predictions, are summarized in Fig. 4(b).

As shown in Fig. 4(b), at $\dot{\epsilon}_H > \dot{\epsilon}_{H2}$, σ_{conf} alone markedly underestimates the total stress. The revised DEMG model accounts for this by including FENE stretching, but consequently overpredicts the steady-state stress even with the friction reduction [35, 69]. Moreover, although previous work has incorporated entanglement loss (Fig. 1(b)), the steady-state stress re-

mains overestimated due to the retention of FENE [40, 41]. Herein, we attribute the stress difference $\Delta\sigma = \sigma_{\text{tot}} - \sigma_{\text{conf}}$ to the frictional stress σ_{fr} that develops during the entangled-to-packed crossover, arising from the strain-induced inter-chain separation along flow. The frictional stress between aligned, unentangled chains is given by $\sigma_{fr,0} \sim \rho \zeta \dot{\epsilon}_H \bar{L}_z^2 / 12$ [32, 55], where \bar{L}_z is the average chain extension along flow and ζ is the monomer friction coefficient (evaluated by a chain dragging method, detailed in the EM). Then, considering that the residual entanglements can suppress the inter-chain separation, the frictional stress can be written as

$$\sigma_{fr} = C \left(\frac{Z}{Z_{\text{equ}}} \right) \frac{\rho \zeta \dot{\epsilon}_H \bar{L}_z^2}{12}, \quad (3)$$

where $C(\cdot)$ is a coefficient depending on the residual entanglements Z normalized by the equilibrium value Z_{equ} . In steady states, Z/Z_{equ} is a small value, enabling an expansion form $C \approx 1 - f Z/Z_{\text{equ}}$. We set $f = 1$ to ensure that $C \approx 0$ at $Z = Z_{\text{equ}}$, where the inter-chain separation along flow is completely suppressed by entangled network. Figure 4(c) demonstrates that this expression for σ_{fr} reproduces $\Delta\sigma$ across varying chain lengths, stiffnesses, and flow rates. In contrast, for entangled states ($\dot{\epsilon}_H < \dot{\epsilon}_{H1}$, $C \approx 0$), the entangled network hinders the inter-chain separation along flow, rendering this frictional stress (and $\Delta\sigma$) negligible, as shown in Fig. 4(a).

According to the above analysis, friction’s role in rheology undergoes a transition due to the entangled-to-packed crossover. Near equilibrium, frictional effect is indirect, “hidden” within the conformational dynamics through controlling the conformational relaxation time [1]. After the crossover, inter-chain separation along flow becomes important due to the exhaustive constraint release and chain alignment, leading to a direct stress contribution from the inter-chain friction. Though some studies have emphasized the role of inter-chain interactions in stress [15, 76–78], this insight has not been incorporated into subsequent tube models. Moreover, some studies imply the dominant role of inter-chain friction in the steady state by employing a picture of “rigid chains”, in which the stress is purely from the inter-chain dissipation [32, 55]. Nevertheless, for non-rigid aligned chains, such as our MD chains, their conformation is dynamically stabilized with intra-chain modes of stretching and retracting, through which the energy is repeatedly stored and released. Thus, the inter-rigid-chain dissipation alone cannot constitute the total stress. By combining both the intra-chain conformation and the inter-chain friction, we nicely quantify the steady-state response.

In summary, we reveal an entangled-to-packed crossover in inter-chain configuration in the nonlinear extension of entangled polymers. Following the saturation of primitive chain stretch, this crossover is accompanied by massive release of entanglements by convection, and finally leads to the steady state, in which the disentangled, aligned chains randomly pack. In the packed state, the tube model fails, while the rheology can be under-

stood by decomposing the stress into a conformational part and a frictional contribution from inter-chain separation, with the latter being long neglected in most theoretical pictures.

We are grateful to Prof. Kröger for helpful discussion and Dr. Yangyang Wang for previous collaboration. This research was supported by National Natural Science Foundation of China (no. 11975136).

-
- [1] Masao Doi and SF Edwards. *The theory of polymer dynamics*, volume 73. oxford university press, 1988.
 - [2] Masao Doi and SF Edwards. Dynamics of concentrated polymer systems. part 2.—molecular motion under flow. *Journal of the Chemical Society, Faraday Transactions 2: Molecular and Chemical Physics*, 74:1802–1817, 1978.
 - [3] Masao Doi and SF Edwards. Dynamics of concentrated polymer systems. part 3.—the constitutive equation. *Journal of the Chemical Society, Faraday Transactions 2: Molecular and Chemical Physics*, 74:1818–1832, 1978.
 - [4] P Schleger, B Farago, C Lartigue, A Kollmar, and D Richter. Clear evidence of reptation in polyethylene from neutron spin-echo spectroscopy. *Physical review letters*, 81(1):124, 1998.
 - [5] Jacob Klein. The onset of entangled behavior in semidilute and concentrated polymer solutions. *Macromolecules*, 11(5):852–858, 1978.
 - [6] G Marrucci. Relaxation by reptation and tube enlargement: A model for polydisperse polymers. *Journal of Polymer Science: Polymer Physics Edition*, 23(1):159–177, 1985.
 - [7] Masao Doi. Explanation for the 3.4-power law for viscosity of polymeric liquids on the basis of the tube model. *Journal of Polymer Science: Polymer Physics Edition*, 21(5):667–684, 1983.
 - [8] ST Milner and TCB McLeish. Reptation and contour-length fluctuations in melts of linear polymers. *Physical Review Letters*, 81(3):725, 1998.
 - [9] D. W. Mead, R. G. Larson, and M. Doi. A molecular theory for fast flows of entangled polymers. *Macromolecules*, 31(22):7895–7914, 1998.
 - [10] Alexei E. Likhtman and Tom C. B. McLeish. Quantitative theory for linear dynamics of linear entangled polymers. *Macromolecules*, 35(16):6332–6343, 2002.
 - [11] Richard S. Graham, Alexei E. Likhtman, Tom C. B. McLeish, and Scott T. Milner. Microscopic theory of linear, entangled polymer chains under rapid deformation including chain stretch and convective constraint release. *Journal of Rheology*, 47(5):1171–1200, 2003.
 - [12] Evelyne Van Ruymbeke, Roland Keunings, Vincent Stéphenne, A Hagenaaers, and Christian Bailly. Evaluation of reptation models for predicting the linear viscoelastic properties of entangled linear polymers. *Macromolecules*, 35(7):2689–2699, 2002.
 - [13] Shi-Qing Wang. *Nonlinear polymer rheology: macroscopic phenomenology and molecular foundation*. John Wiley & Sons, 2018.
 - [14] Zhe Wang, Christopher N Lam, Wei-Ren Chen, Weiyu Wang, Jianning Liu, Yun Liu, Lionel Porcar, Christopher B Stanley, Zhichen Zhao, Kunlun Hong, et al. Fingerprinting molecular relaxation in deformed polymers. *Physical Review X*, 7(3):031003, 2017.
 - [15] Alexei E. Likhtman. Whither tube theory: From believing to measuring. *Journal of Non-Newtonian Fluid Mechanics*, 157(3):158–161, 2009.
 - [16] Nicolas J. Alvarez, Qian Huang, Ole Hassager, and Sara L. Wingstrand. Linear and nonlinear universality in the rheology of polymer melts and solutions. *Physical Review Letters*, 115(7):078302, 2015.
 - [17] John M Dealy, Daniel J Read, and Ronald G Larson. *Structure and rheology of molten polymers: from structure to flow behavior and back again*. Carl Hanser Verlag GmbH Co KG, 2018.
 - [18] Yumi Matsumiya and Hiroshi Watanabe. Non-universal features in uniaxially extensional rheology of linear polymer melts and concentrated solutions: A review. *Progress in Polymer Science*, 112:101325, 2021.
 - [19] Anders Bach, Kristoffer Almdal, Henrik Koblitzi Rasmussen, and Ole Hassager. Elongational viscosity of narrow molar mass distribution polystyrene. *Macromolecules*, 36(14):5174–5179, 2003.
 - [20] P. K. Bhattacharjee, J. P. Oberhauser, G. H. McKinley, L. G. Leal, and T. Sridhar. Extensional rheometry of entangled solutions. *Macromolecules*, 35(27):10131–10148, 2002.
 - [21] P. K. Bhattacharjee, D. A. Nguyen, G. H. McKinley, and T. Sridhar. Extensional stress growth and stress relaxation in entangled polymer solutions. *Journal of Rheology*, 47(1):269–290, 2003.
 - [22] Alexis André, Taisir Shahid, Filip Oosterlinck, Christian Clasen, and Evelyne Van Ruymbeke. Investigating the transition between polymer melts and solutions in nonlinear elongational flow. *Macromolecules*, 54(6):2797–2810, 2021.
 - [23] Giuseppe Marrucci and Giovanni Ianniruberto. Inter-chain pressure effect in extensional flows of entangled polymer melts. *Macromolecules*, 37(10):3934–3942, 2004.
 - [24] Manfred H. Wagner, Saeid Kheirandish, and Ole Hassager. Quantitative prediction of transient and steady-state elongational viscosity of nearly monodisperse polystyrene melts. *Journal of Rheology*, 49(6):1317–1327, 2005.
 - [25] Esmaeil Narimissa, Qian Huang, and Manfred H. Wagner. Elongational rheology of polystyrene melts and solutions: Concentration dependence of the interchain tube pressure effect. *Journal of rheology*, 64(1):95–110, 2020.
 - [26] Masao Doi and Hiroshi Watanabe. Effect of nematic interaction on the rouse dynamics. *Macromolecules*, 24(3):740–744, 1991.
 - [27] Jing Cao and Alexei E. Likhtman. Time-dependent orientation coupling in equilibrium polymer melts. *Phys Rev Lett*, 104(20):207801, 2010.
 - [28] Gun Woo Park and Giovanni Ianniruberto. Flow-induced nematic interaction and friction reduction successfully describe ps melt and solution data in extension startup and relaxation. *Macromolecules*, 50(12):4787–4796, 2017.
 - [29] G. Ianniruberto, A. Brasiello, and G. Marrucci. Simulations of fast shear flows of ps oligomers confirm monomeric friction reduction in fast elongational flows of

- monodisperse ps melts as indicated by rheoptical data. *Macromolecules*, 45(19):8058–8066, 2012.
- [30] Takatoshi Yaoita, Takeharu Isaki, Yuichi Masubuchi, Hiroshi Watanabe, Giovanni Ianniruberto, and Giuseppe Marrucci. Primitive chain network simulation of elongational flows of entangled linear chains: Stretch/orientation-induced reduction of monomeric friction. *Macromolecules*, 45(6):2773–2782, 2012.
- [31] Yuichi Masubuchi, Takatoshi Yaoita, Yumi Matsumiya, Hiroshi Watanabe, Giovanni Ianniruberto, and Giuseppe Marrucci. Stretch/orientation induced acceleration in stress relaxation in coarse-grained molecular dynamics simulations. *Nihon Reorji Gakkaishi*, 41(1):35–37, 2013.
- [32] Giovanni Ianniruberto and Giuseppe Marrucci. Molecular dynamics reveals a dramatic drop of the friction coefficient in fast flows of polymer melts. *Macromolecules*, 53(7):2627–2633, 2020.
- [33] Sai Vineeth Bobbili and Scott T. Milner. Chain tension reduces monomer friction in simulated polymer melts. *Journal of Rheology*, 64(6):1373–1378, 2020.
- [34] Yumi Matsumiya, Hiroshi Watanabe, Yuichi Masubuchi, Qian Huang, and Ole Hassager. Nonlinear elongational rheology of unentangled polystyrene and poly (p-tert-butylstyrene) melts. *Macromolecules*, 51(23):9710–9729, 2018.
- [35] Salvatore Costanzo, Qian Huang, Giovanni Ianniruberto, Giuseppe Marrucci, Ole Hassager, and Dimitris Vlassopoulos. Shear and extensional rheology of polystyrene melts and solutions with the same number of entanglements. *Macromolecules*, 49(10):3925–3935, 2016.
- [36] Céline Hannecart, Taisir Shahid, Dimitris Vlassopoulos, Filip Oosterlinck, Christian Clasen, and Evelyn van Ruymbeke. Decoding the steady elongational viscosity of monodisperse linear polymers using tube-based modeling. *Journal of Rheology*, 66(1):197–218, 2022.
- [37] Chunggi Baig, Vlas G. Mavrantzas, and Martin Kröger. Flow effects on melt structure and entanglement network of linear polymers: Results from a nonequilibrium molecular dynamics simulation study of a polyethylene melt in steady shear. *Macromolecules*, 43(16):6886–6902, 2010.
- [38] Ziwei Liu, Tingyu Xu, Fan Peng, Renkuan Cao, Hao Sun, Yunhan Zhang, and Liangbin Li. Improved predictions of nonlinear uniaxial tensile stress in polymer melts by accounting for microscopic conformation and entanglement changes. *J Chem Phys*, 162(20), 2025.
- [39] Yangyang Wang and Shi-Qing Wang. Salient features in uniaxial extension of polymer melts and solutions: Progressive loss of entanglements, yielding, non-gaussian stretching, and rupture. *Macromolecules*, 44(13):5427–5435, 2011.
- [40] Giovanni Ianniruberto and Giuseppe Marrucci. Convective constraint release (ccr) revisited. *Journal of Rheology*, 58(1):89–102, 2014.
- [41] Giovanni Ianniruberto. Quantitative appraisal of a new ccr model for entangled linear polymers. *Journal of Rheology*, 59(1):211–235, 2015.
- [42] Kurt Kremer and Gary S. Grest. Dynamics of entangled linear polymer melts: A molecular-dynamics simulation. *The Journal of Chemical Physics*, 92(8):5057–5086, 1990.
- [43] Steve Plimpton. Fast parallel algorithms for short-range molecular dynamics. *Journal of Computational Physics*, 117(1):1–19, 1995.
- [44] Hsiao-Ping Hsu and Kurt Kremer. Static and dynamic properties of large polymer melts in equilibrium. *The Journal of Chemical Physics*, 144(15), 2016.
- [45] Rolf Auhl, Ralf Everaers, Gary S. Grest, Kurt Kremer, and Steven J. Plimpton. Equilibration of long chain polymer melts in computer simulations. *The Journal of Chemical Physics*, 119(24):12718–12728, 2003.
- [46] Matthew Dobson. Periodic boundary conditions for long-time nonequilibrium molecular dynamics simulations of incompressible flows. *The Journal of Chemical Physics*, 141(18):184103, 2014.
- [47] Thomas A. Hunt. Periodic boundary conditions for the simulation of uniaxial extensional flow of arbitrary duration. *Molecular Simulation*, 42(5):347–352, 2016.
- [48] David A Nicholson and Gregory C Rutledge. Molecular simulation of flow-enhanced nucleation in n-eicosane melts under steady shear and uniaxial extension. *The Journal of chemical physics*, 145(24), 2016.
- [49] Livia A. Moreira, Guojie Zhang, Franziska Müller, Torsten Stuehn, and Kurt Kremer. Direct equilibration and characterization of polymer melts for computer simulations. *Macromolecular Theory and Simulations*, 24(5):419–431, 2015.
- [50] Muhammad Anwar and Richard S Graham. Nonlinear shear of entangled polymers from nonequilibrium molecular dynamics. *Journal of Polymer Science Part B: Polymer Physics*, 57(24):1692–1704, 2019.
- [51] Martin Kröger, Joseph D. Dietz, Robert S. Hoy, and Clarisse Luap. The z1+ package: Shortest multiple disconnected path for the analysis of entanglements in macromolecular systems. *Computer Physics Communications*, 283:108567, 2023.
- [52] Kenneth S. Schweizer and Shi-Jie Xie. Physics of the stress overshoot and chain stretch dynamics of entangled polymer liquids under continuous startup nonlinear shear. *ACS Macro Letters*, 7(2):218–222, 2018.
- [53] Shi-Jie Xie and Kenneth S. Schweizer. Consequences of delayed chain retraction on the rheology and stretch dynamics of entangled polymer liquids under continuous nonlinear shear deformation. *Macromolecules*, 51(11):4185–4200, 2018.
- [54] Shi-Qing Wang, Sham Ravindranath, Yangyang Wang, and Pouyan Boukany. New theoretical considerations in polymer rheology: Elastic breakdown of chain entanglement network. *The Journal of Chemical Physics*, 127(6):064903, 2007.
- [55] Thomas C. O’Connor, Nicolas J. Alvarez, and Mark O. Robbins. Relating chain conformations to extensional stress in entangled polymer melts. *Phys Rev Lett*, 121(4):047801, 2018.
- [56] G Marrucci. Dynamics of entanglements: A nonlinear model consistent with the cox-merz rule. *Journal of non-newtonian fluid mechanics*, 62(2-3):279–289, 1996.
- [57] Alexei E Likhtman, Scott T Milner, and Tom CB McLeish. Microscopic theory for the fast flow of polymer melts. *Physical review letters*, 85(21):4550, 2000.
- [58] DJ Read. Convective constraint release with chain stretch: Solution of the rouse-tube model in the limit of infinite tubes. *Journal of Rheology*, 48(2):349–377, 2004.
- [59] Lin-Feng Wu, Long-Fei Mao, and Zhe Wang. Effective entanglement and constraint release in deformed polymer melts. *Macromolecules*, 57(7):3202–3211, 2024.
- [60] Yongjin Ruan, Yuyuan Lu, Lijia An, and Zhen-Gang Wang. Multiple entanglements between two chains in polymer melts: An analysis of primitive paths based on frenet trihedron. *Macromolecules*, 57(6):2792–2800, 2024.

- [61] Hsiao-Ping Hsu and Kurt Kremer. Clustering of entanglement points in highly strained polymer melts. *Macromolecules*, 52(17):6756–6772, 2019.
- [62] Hsiao-Ping Hsu and Kurt Kremer. Primitive path analysis and stress distribution in highly strained macromolecules. *ACS Macro Letters*, 7(1):107–111, 2018.
- [63] Yexin Zheng, Mesfin Tsige, and Shi Qing Wang. Molecular dynamics simulation of entangled melts at high rates: Identifying entanglement lockup mechanism leading to true strain hardening. *Macromolecular Rapid Communications*, 44(1), 2023.
- [64] Soroush Moghadam, Indranil Saha Dalal, and Ronald G. Larson. Unraveling dynamics of entangled polymers in strong extensional flows. *Macromolecules*, 52(3):1296–1307, 2019.
- [65] D. E. Smith and S. Chu. Response of flexible polymers to a sudden elongational flow. *Science*, 281(5381):1335–40, 1998.
- [66] Ángel Mulero. *Theory and simulation of hard-sphere fluids and related systems*, volume 753. Springer, 2008.
- [67] Carlos R López-Barrón, Yiming Zeng, Jonathan J Schaefer, Aaron PR Eberle, Timothy P Lodge, and Frank S Bates. Molecular alignment in polyethylene during cold drawing using in-situ sans and raman spectroscopy. *Macromolecules*, 50(9):3627–3636, 2017.
- [68] Thomas C O’Connor, Austin Hopkins, and Mark O Robbins. Stress relaxation in highly oriented melts of entangled polymers. *Macromolecules*, 52(22):8540–8550, 2019.
- [69] Priyanka S. Desai and Ronald G. Larson. Constitutive model that shows extension thickening for entangled solutions and extension thinning for melts. *Journal of Rheology*, 58(1):255–279, 2014.
- [70] D. Pearson, E. Herbolzheimer, N. Grizzuti, and G. Marrucci. Transient behavior of entangled polymers at high shear rates. *Journal of polymer science. Part B, Polymer physics*, 29(13):1589–1597, 1991.
- [71] Clarisse Luap, Christian Müller, Thomas Schweizer, and David C. Venerus. Simultaneous stress and birefringence measurements during uniaxial elongation of polystyrene melts with narrow molecular weight distribution. *Rheologica Acta*, 45(1):83–91, 2005.
- [72] J. Gao and J. H. Weiner. Monomer-level description of stress and birefringence relaxation in polymer melts. *Macromolecules*, 27(5):1201–1209, 1994.
- [73] Jing Cao and Alexei E. Likhtman. Simulating startup shear of entangled polymer melts. *ACS Macro Letters*, 4(12):1376–1381, 2015.
- [74] Hiroshi Watanabe, Yumi Matsumiya, and Tadashi Inoue. Revisit the stress-optical rule for entangled flexible chains: Overshoot of stress, segmental orientation, and chain stretch on start-up of flow. *Nihon Reorogi Gakkaishi*, 43(34):105–112, 2015.
- [75] Carlos R López-Barrón, Wesley R Burghardt, and Mu Sung Kweon. Local and global stretching of polymer chains during startup of extensional flow. *ACS Macro Letters*, 9(1):26–31, 2019.
- [76] Jianping Gao and Jerome H Weiner. Nature of stress on the atomic level in dense polymer systems. *Science*, 266(5186):748–752, 1994.
- [77] Jorge Ramírez, Sathish K. Sukumaran, and Alexei E. Likhtman. Significance of cross correlations in the stress relaxation of polymer melts. *The Journal of Chemical Physics*, 126(24):244904, 2007.
- [78] J. Gao and J. H. Weiner. Range of validity of the entropic spring concept in polymer melt relaxation. *Macromolecules*, 25(13):3462–3467, 1992.

End Matter

Appendix A: Simulation – Simulations of entangled polymer melts are based on the standard Kremer–Grest model [44]. Nonbonded monomers interact via the WCA potential $U_{\text{WCA}} = 4\epsilon \left[\left(\frac{\sigma}{r} \right)^{12} - \left(\frac{\sigma}{r} \right)^6 + \frac{1}{4} \right]$ for $r < 2^{1/6}\sigma$, and 0 otherwise. Consecutive beads with mean bond length $b = 0.964$ are connected by the FENE potential $U_{\text{FENE}} = -\frac{1}{2}kR_0^2 \ln \left[1 - \left(\frac{r}{R_0} \right)^2 \right]$ with $k = 30\epsilon/\sigma^2$ and $R_0 = 1.5\sigma$. Chain stiffness is introduced through $U_{\text{bend}} = k_{\text{bc}}(1 - \cos\alpha)$, where α is the bond angle. We simulate $N_c = 250$ or 200 chains of length $N = 300$ or 500 at a fixed monomer density $\rho = N_c N/V = 0.85\sigma^{-3}$. Equilibrated configurations are generated using a Monte Carlo bond-swap algorithm [45] and validated against established benchmarks [44]. For $k_{\text{bc}} = 0, 0.75$, and 1.5 , the entanglement lengths are $N_e \approx 60, 51$ and 28 , corresponding to entanglement times $\tau_e \approx 3290\tau, 2800\tau$ and 1980τ , respectively [44, 49, 50, 73]. Rouse and reptation times are estimated as $\tau_R = \tau_e(N/N_e)^2$ and $\tau_d = 3\tau_e(N/N_e)^3$, with the plateau modulus $G_N^0 = \frac{4}{5} \frac{\rho k_B T}{N_e}$, where k_B is Boltzmann constant. Flow is imposed via the SLLOD equations of motion, combined with a Nosé–Hoover thermostat and the generalized Kraynik–Reinelt boundary condition [46–48].

Appendix B: Convective SEE release – To model the release of SEE, we regard a Z-fold PP as being connected to an elastic plate that deforms affinely with ϵ_H . SEEs are treated as rings pinned to the plate (Fig. 5(a)). As the plate elongates, rings slide along the PP and are released once reaching a chain end (Fig. 5(a)). Here we introduce a threshold strain ϵ_{HR} , in the sense that for $\epsilon_H > \epsilon_{\text{HR}}$ the generation of new SEE is ignorable. ϵ_{HR} is larger than ϵ_{H1} . We then consider the convective release of SEE at $\epsilon_H > \epsilon_{\text{HR}}$. Let $x(t') = \frac{Z_{\text{SEE}}(\epsilon_{\text{HR}} + \dot{\epsilon}_H t')}{Z_{\text{SEE}}(\epsilon_{\text{HR}})}$ denote the fraction of remaining SEE at time t' (the origin of time is set as the moment the PP elongates to $\epsilon_H = \epsilon_{\text{HR}}$). Considering a SEE at the contour coordinate $s = x(t')L_{\text{sc}}$ at $t = 0$, where L_{sc} is the half length of PP, and the origin of s is at the center of PP. At $t = t'$, it just reaches the end of PP ($s = L_{\text{sc}}$). It is easy to see that SEEs with $s < x(t')L_{\text{sc}}$ at $t = 0$ will survive at $t = t'$, while those with $s > x(t')L_{\text{sc}}$ at $t = 0$ will release at $t = t'$. From $t = 0$ to t' , the plate elongates with the ratio $\lambda = \exp(\dot{\epsilon}_H t')$. Then, it is found that $\lambda = \exp(\dot{\epsilon}_H t') = \frac{L_{\text{sc}}}{x(t')L_{\text{sc}}} = \frac{1}{x(t')}$, which gives $x(t) = \exp(-\dot{\epsilon}_H t)$. Note that this result is based on the assumption that PP length is fixed. In fact, even at $\epsilon_H > \epsilon_{\text{HR}}$, PP length still mildly increases with strain. To correct this problem, we can incorporate the stretch of PP $\lambda_{\text{pp}}(t) = \bar{L}_{\text{pp}}(t)/\bar{L}_{\text{pp}}(0)$, which results in:

$$x(t) = \frac{\lambda_{\text{pp}}(\epsilon_{\text{HR}} + \dot{\epsilon}_H t)}{\lambda_{\text{pp}}(\epsilon_{\text{HR}})} \cdot \frac{1}{\exp(\dot{\epsilon}_H t)}, \quad (\text{B1})$$

λ_{pp} can be obtained from MD data. Using $\epsilon_{\text{HR}} = 2.2$, Fig. 5(b) compares the MD results of the sample with

$k_{\text{bc}} = 1.5$, $N = 500$ and $Wi_R = 40$ with predictions of eq. B1 for four different Wi_R values. All model curves collapse onto a master curve and agree with the simulation results, demonstrating that SEE release is governed by convection.

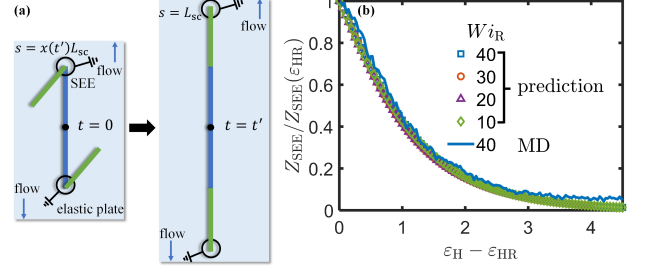


FIG. 5. Geometric mechanism of SEE release for a sample with $N = 500$ and $k_{\text{bc}} = 1.5$. (a) Illustration of SEE sliding and release along the primitive path during affine deformation of a Z-fold chain. (b) Remaining SEE fraction for $\epsilon_{\text{HR}} = 2.2$: MD results compared to analytic predictions ($Wi_R = 10$ –40).

Appendix C: $g_{2D}(\mathbf{r})$ – We slice the simulation box along z -axis with each slice having a thickness of $\sqrt{N_e}b$. For each slice, the centers of mass of chain segments contained in this slice are projected onto the x - y plane (Fig. 6), resulting in the projected coordinate sets $\{\mathbf{r}_l\}$. Then, its $g_{2D}(\mathbf{r})$ is given by

$$\rho_{2D} g_{2D}(\mathbf{r}) = \frac{1}{N_{2D}} \sum_{l=1}^{N_{2D}} \sum_{l' \neq l}^{N_{2D}} \langle \delta[\mathbf{r} + \mathbf{r}_l - \mathbf{r}_{l'}] \rangle. \quad (\text{C1})$$

where N_{2D} is the number of projected points and ρ_{2D} is the 2D density of projected points for the slice. The $g_{2D}(\mathbf{r})$ of the system is found by averaging the results from all slices. With $g_{2D}(\mathbf{r})$, I_{1s} is found by $I_{1s} = 2\pi\rho_{2D} \int_0^{r_{\text{min}}} g_{2D}(r)r dr$, where r_{min} is the position of $g_{2D}(\mathbf{r})$'s first minimum.

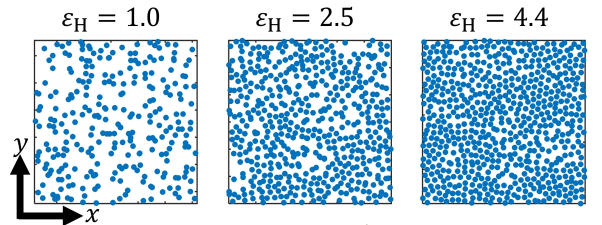


FIG. 6. Snapshot of x – y plane and the corresponding projected centers-of-mass $\{\mathbf{r}_l\}$ of chain segments, for a sample with $N = 500$, $k_{\text{bc}} = 1.5$ and $Wi_R = 40$ at $\epsilon_H = 1.0, 2.5$ and 4.4 .

Appendix D: DEMG model – The differential form of the DEMG model without friction reduction is given by [69, 70]:

$$\overset{\nabla}{\mathbf{S}} = -2(\boldsymbol{\kappa} : \mathbf{S})\mathbf{S} - \frac{1}{\lambda^2 \tau_d} \left(\mathbf{S} - \frac{\boldsymbol{\delta}}{3} \right), \quad (\text{D1})$$

$$\frac{d\lambda}{dt} = \lambda(\boldsymbol{\kappa} : \mathbf{S}) - \frac{k_s(\lambda - 1)}{\tau_R}, \quad (\text{D2})$$

$$\boldsymbol{\sigma} = 3G_N^0 k_s \lambda^2 \mathbf{S}. \quad (\text{D3})$$

Here, \mathbf{S} and λ denote the tube orientation tensor and stretch ratio, respectively; $\overset{\nabla}{\mathbf{S}}$ represents the upper-convected derivative, $\boldsymbol{\kappa}$ is the transpose of the velocity gradient tensor, and $\boldsymbol{\delta}$ is the unit tensor. Model parameters τ_R , τ_d and G_N^0 are matched to our simulated systems. The nonlinear spring coefficient k_s is given by the inverse Langevin function approximation, $k_s = \frac{(3\lambda_{\max}^2 - \lambda^2)/(\lambda_{\max}^2 - \lambda^2)}{(3\lambda_{\max}^2 - 1)/(\lambda_{\max}^2 - 1)}$, where the $\lambda_{\max} = \frac{N_e b}{\sqrt{N_e} b} = \sqrt{N_e}$ is the maximum stretch ratio of chain.

To incorporate flow-induced friction reduction, the relaxation times reduce according to $\tau_R = \tau_R^0 \zeta(F_{\text{so}})$ and $\tau_d = \tau_d^0 \zeta(F_{\text{so}})$, where τ_R^0 and τ_d^0 are equilibrium values, and the friction reduction factor is $\zeta(F_{\text{so}}) = \left(1 - \frac{\lambda^4}{\lambda_{\max}^4} (\mathbf{S} : \mathbf{S})\right)^2$ [69].

Appendix E: Monomer friction coefficient – For undeformed entangled systems, monomer friction can be found by the fluctuation–dissipation theorem, where the diffusion coefficient is measured and converted to ζ using the Einstein relation [32, 33]. In steady states, chains are disentangled and aligned. In this case, inter-chain separation along flow becomes significant. Thus, we can directly determine ζ via a chain dragging method. To find ζ at a strain ε_H ($\varepsilon_H > \varepsilon_{H2}$), we drag a test chain with length N_t along z axis in the stretched environment composed of stretched surrounding chains. To generate these surrounding chains, we stretch the sample to ε_H ,

and then fix the end beads of all chains to keep their orientations and stretching at ε_H . The test chain is subjected to a pair of balanced forces applied at its two ends, respectively along z and $-z$ directions. The magnitude of this balanced force is adjusted to keep the stretch ratio of the test chain consistent with those of the chain segments of the same length N_t in the sample stretched to ε_H . Uniform drag forces F are applied to every bead of the test chain along the flow direction with the same magnitude. The simulation is thermostatted using the Nosé–Hoover thermostat. As shown in Fig. 7(a) for the case of $N_t = 500$ and $\varepsilon_H = 6$, the center-of-mass velocity v of test chain along flow direction increases linearly with the applied drag force F , confirming the validity of the linear friction law. Additionally, we find that the extracted monomer friction coefficient ζ is not sensitive to N_t for $N_t \geq N_e$ (Fig. 7(b)), suggesting that our result is reliable.

We also evaluate ζ by measuring the diffusion coefficient along flow direction [32, 33]. It is seen that the result is consistent with the ζ found by the chain dragging method at a semi-quantitative level.

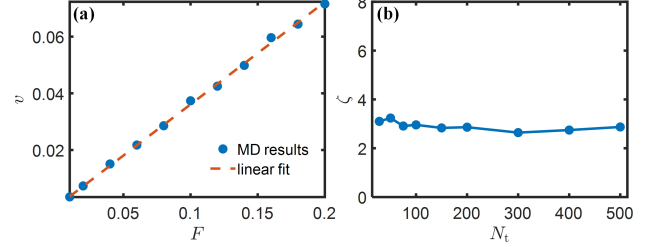


FIG. 7. Chain-dragging results for the sample with $N = 500$, $k_{bc} = 1.5$ and $Wi_R = 40$ at $\varepsilon_H = 6.0$. (a) Applied force F vs center-of-mass velocity v of a test chain with $N_t = 500$; symbols: MD results, dashed line: fit of $v = \frac{1}{\zeta} F$ (b) Extracted monomer friction coefficient ζ as a function of N_t at fixed $F = 0.08$, showing a plateau for $N_t \geq N_e$.